

OPEN

# A thin film efficient pn-junction thermoelectric device fabricated by self-align shadow mask

Gilbert Kogo<sup>1\*</sup>, Bo Xiao<sup>1</sup>, Samuel Danquah<sup>1</sup>, Harold Lee<sup>1</sup>, Julien Niyogushima<sup>1</sup>, Kelsea Yarbrough<sup>1</sup>, Aaditya Candadai<sup>2</sup>, Amy Marconnet<sup>2</sup>, Sangram K. Pradhan<sup>1\*</sup> & Messaoud Bahoura<sup>1,3</sup>

Large area highly crystalline MoS<sub>2</sub> and WS<sub>2</sub> thin films were successfully grown on different substrates using radio-frequency magnetron sputtering technique. Structural, morphological and thermoelectric transport properties of MoS<sub>2</sub> and WS<sub>2</sub> thin films have been investigated systematically to fabricate high-efficient thermal energy harvesting devices. X-ray diffraction data revealed that crystallites of MoS<sub>2</sub> and WS<sub>2</sub> films are highly oriented in 002 plane with uniform grain size distribution confirmed through atomic force microscopy study. Surface roughness increases with substrate temperature and it plays a big role in electron and phonon scattering. Interestingly, MoS<sub>2</sub> films also display low thermal conductivity at room temperature and strongly favors achievement of higher thermoelectric figure of merit value of up to 1.98. Raman spectroscopy data shows two distinct MoS<sub>2</sub> vibrational modes at 380 cm<sup>-1</sup> for E<sub>12g</sub> and 410 cm<sup>-1</sup> for A<sub>1g</sub>. Thermoelectric transport studies further demonstrated that MoS<sub>2</sub> films show p-type thermoelectric characteristics, while WS<sub>2</sub> is an n-type material. We demonstrated high efficient pn-junction thermoelectric generator device for waste heat recovery and cooling applications.

Global energy consumption is increasing day by day due to industrial and high population growth. There is a major global challenge in striving to meet the future energy demand in renewable, sustainability, clean, and safe energy sources<sup>1,2</sup>. One way in improving the electricity demand is by scavenging waste heat using thermoelectric generators<sup>3</sup>. The conversion of waste heat into electricity will provide alternative energy that will reduce our dependence on fossil fuels and reduce greenhouse gas emissions<sup>4</sup>. The performance of thermoelectric energy conversion devices depends on thermoelectric figure of merit  $ZT$  (Eq. 1), where  $S$ ,  $\sigma$ ,  $\kappa_{total} = \kappa_e + \kappa_p$ , and  $T$  are the Seebeck coefficient, electrical conductivity, total thermal conductivity, and absolute temperature, respectively<sup>5</sup>. Thermal conductivity comes from two sources: (1) electrons and holes transporting heat  $\kappa_e$  and (2) phonons travelling through the lattice  $\kappa_l$ <sup>6</sup>.

$$ZT = \frac{S^2 \sigma}{\kappa_{total}} \quad (1)$$

According to the figure of merit, good thermoelectric materials should possess high  $S$  value to have high voltage output, high  $\sigma$  value to reduce Joule heating, and low  $\kappa$  value to maintain large temperature difference<sup>2</sup>. Among the four quantities in Eq. (1) above,  $S$ ,  $\sigma$ , and  $\kappa_e$  are interrelated to the electronic structure of the material, and  $\kappa_l$  is mainly related to the lattice vibration<sup>7</sup>. One possible way to improve the figure of merit is to reduce the lattice thermal conductivity without significantly altering the electronic properties of the material<sup>8</sup>.

The Seebeck coefficient is mostly considered as a bulk materials property. The figure of merit for most efficient bulk semiconductor (Bi<sub>2</sub>Te<sub>3</sub>, Sb<sub>2</sub>Te<sub>3</sub>) based device has been stable over the past several decades, with  $ZT$  value close to 1 and efficiency is about 10% of the Carnot limit. By reducing the size of the materials from 3D to lower dimension, the effect of interface becomes more significant as the hot and cold junctions are closer to each other and therefore the Seebeck coefficient is not independent of size anymore. Theoretical study proposed by other group shows that the reduced dimensionality of heterostructure/superlattice could be used to enhance the

<sup>1</sup>Center for Materials Research, Norfolk State University, Norfolk, Virginia, 23504, USA. <sup>2</sup>Mechanical Engineering Purdue University, West Lafayette, In 47907, USA. <sup>3</sup>Department of Engineering, Norfolk State University, Norfolk, Virginia, 23504, USA. \*email: [g.kogo@spartans.nsu.edu](mailto:g.kogo@spartans.nsu.edu); [skpradhan@nsu.edu](mailto:skpradhan@nsu.edu)

electronic density of state<sup>9–12</sup>. Hence, the mean free path of electron is longer in thin films compared to the one in the bulk material. Consequently, the electrons energies remain high because they do not get sufficient time to thermalize with the lattice.

Currently, the possibility of tailoring thermal and electrical properties offered by the heterostructure materials has attracted considerable attention. The strategy of rationally engineering semiconductor interfaces could enhance the ZT in thermoelectric (TE) materials with heterostructures. In these heterostructures, the significant enhancement performance is believed to result from the growth by preferential scattering of low-energy carriers more effectively than high ones and the reduction of the thermal conduction via scattering phonons at the heterostructured interfaces<sup>13–15</sup>. So far, the maximum reported room-temperature ZT to date, ~2.4 by Venkatasubramanian *et al.*, was reached using superlattice heterostructure made up of *p*-type Bi<sub>2</sub>Te<sub>3</sub>/Sb<sub>2</sub>Te<sub>3</sub> and was attributed to good electrical transport and very low thermal conductivity<sup>16</sup>. Although, Bi<sub>2</sub>Te<sub>3</sub> and Sb<sub>2</sub>Te<sub>3</sub> are more promising materials and the device made out of it are showing highest figure of merit, but they are very toxic, carcinogenic in nature and are not bio friendly.

As an alternative bio-friendly materials, the transition metal dichalcogenides recently shows very promising waste heat conversion performance by limiting its thickness to one layer or multiple layers and, more attentions are given to MoS<sub>2</sub>, MoSe<sub>2</sub>, WS<sub>2</sub>, WSe<sub>2</sub>, and so on<sup>17–21</sup>. Among these materials, the electronic band structure of monolayer or bi layers thickness of MoS<sub>2</sub> and WS<sub>2</sub> show an excellent carrier mobility compare to the bulk and exhibit the band tunability from indirect to direct band gap semiconductor<sup>22</sup>. Hence, the electronic device made out of these materials shows exceptional device performance and these nano sheet are very good thermal insulator and favor to prevent the heat flow during operation<sup>23–25</sup>. Similarly, previous study based on theoretical calculation emphasized that the single layer of WS<sub>2</sub> and MoS<sub>2</sub> films also show higher value of thermoelectric figure of merit known as ZT<sup>18,19,21</sup>. The high figure of merit in few layers of MoS<sub>2</sub>/WS<sub>2</sub> heterostructure are considered as one of the potential thermoelectric materials for optimum waste heat energy harvesting.

The thermoelectric device performance and its waste heat conversion efficiency can be derived from ZT and Carnot efficiency using the following equation as below<sup>2,26–28</sup>.

$$\eta_{TEG} = \left( \frac{T_h - T_c}{T_h} \right) \left[ \frac{\sqrt{1 + ZT_M} - 1}{\sqrt{1 + ZT_M} + \frac{T_c}{T_h}} \right] \quad (2)$$

where  $T_c$  and  $T_h$  is the temperature at cold and warm side respectively,  $Z T_M$  represents the materials optimum figure of merits among the cold and hot temperature end. Current research in thermoelectric devices is based on power generation that utilizes Seebeck effect, and cooling is achieved through Peltier effect. Very small/minature version of thermoelectric device has more demand for cooling of several electronic circuit that brings in fabrication of thin film-based devices to meet the need for integrated circuit, and optical fiber communications technology<sup>28,29</sup>. Further, by lowering the dimensionality, materials properties such as  $S$ ,  $\sigma$ , and  $\kappa$  can be controlled by tuning the lengthscale<sup>26</sup>.

The most popular design of thermoelectric modules used for waste heat harvesting are either planar or vertical style. Planar modules helps to build up the temperature gradient in the plane whereas the temperature difference can generated across the film thickness of the thermoelectric materials<sup>30</sup>. The formation of electrical contacts for planar type is simple compared to vertical type, and the device fabricated using a very low thermal conductivity substrate favor to create huge temperature difference in planar type module for optimum performance<sup>30</sup>. The device fabrication is cost effective as compared to other expensive processes where etching, photoresist and MEMS technologies are required. These limitations can be overcome by employing self-aligned shadow masking technique where the film deposition and TE modules are made in three stages: first one for negative semiconducting plane, second one for positive semiconducting plane, whereas third one is the electrical contacts that can connect both plane. The high vacuum and high substrate temperature favor to grow good quality film which is of prime importance to obtain the higher thermo-electric figure of merit<sup>29</sup>.

The development of temperature gradient for thin films structure is higher than the bulk counterpart module during the operation at same thermal condition, therefore, few layer thick films are ideal since larger temperature difference is required for high efficiency thermoelectric device<sup>26,30,31</sup>. The planar thin film module device design plays an important role in improving the efficiency of the TE device. Thermoelectric generators are connected electrically in series and thermally in parallel, this means the contacts at the hot end and cold end is the main factor that determines the efficiency of the TE device<sup>32</sup>. The current design, where metal electrode bonding on hot side, causes mechanical stress and unavoidable temperature drops across the substrates causing drawbacks of thermoelectric generator (TEG)<sup>33</sup>. Additionally, the design causes mismatch of the coefficient of thermal expansion between the metal-semiconductor interface at high temperatures, mechanically induced failure, chemical instability and diffusion of atoms across the interfaces<sup>34</sup>. In this paper, the design is based on pn-junction TEG, where the p-type and n-type planner patterns are connected directly at the hot end forming a pn-junction, and electrical contacts on the cold side. The design will alleviate the issues mentioned above and generate electron-hole pairs in space charge region, thus, contributing to thermoelectric device efficiency<sup>35</sup>. Figure 1 shows the schematic of pn-junction TEG.

In this paper, a pn-junction thermoelectric device for waste heat recovery and cooling was fabricated by RF magnetron sputtering of MoS<sub>2</sub> and WS<sub>2</sub> films on glass substrate at substrate temperatures that gave their individual high thermoelectric transport properties.

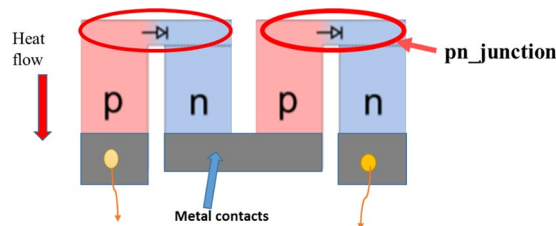


**Figure 1.** Schematic of pn-junction thermoelectric generator.

## Experimental Procedures

**Thin film deposition.** MoS<sub>2</sub> and WS<sub>2</sub> films were deposited by RF magnetron sputtering on glass, sapphire and silicon substrates at several substrate temperatures, RF power, and argon pressure. Molybdenum disulfide (MoS<sub>2</sub>) and tungsten disulfide (WS<sub>2</sub>) targets with purity of 99.9% pure with a diameter of 3 inches by 0.125 inches thick, and indium bonded to copper backing plate were made by Kurt J. Lesker company. For electrical properties measurement, chromium electrodes were deposited on glass, sapphire substrates via thermal evaporation. The temperature difference voltage measurement was performed in indigenously developed test apparatus in the laboratory.

**Structural properties.** Structural properties of the films studied using Rigaku X-ray diffractometer, using copper K<sub>α</sub> source. Surface morphology and domain distribution of the films were characterized using atomic force microscope in tapping mode. X-ray photoelectron spectroscopy analysis of the film was performed to identify the chemical/oxidation state of the film. Vibrational modes were determined using HR Raman spectroscopy.

**Device fabrication.** Figure 2a illustrates a step by step procedure to fabricate the thermoelectric device using steel shadow mask and substrate pocket.

All the masks were designed using Autodesk inventor 2017 software, and steel were cut using expert mill at local workshop, Norfolk technical center, Norfolk, Virginia. Different masks are prepared with specific aperture dimensions to specify the profile of the thermoelectric legs and their metallic contacts for electrical measurement. We also focused the proper alignment of the mask during the device fabrication by securely tighten the four corner screw of 0.125 cm radius. The size of both semiconducting planner leg dimensions were 3.2 cm long and 0.317 cm wide. Whereas for proper electrical contact between two planar legs, the size of the metal contacts are 0.317 cm and 0.785 cm on its width and length, respectively, as shown in Fig. 2e,f. The individual planar patterns devices were placed 0.15 cm apart. The size of our entire thermoelectric structure with multiple planar legs was 7.5 cm × 3.6 cm<sup>35</sup>. Both MoS<sub>2</sub> and WS<sub>2</sub> films are deposited at the substrate temperature of 450 °C and annealed at 600 °C in Argon environments for 1 hour. The beginning step start with WS<sub>2</sub> semiconducting planar leg of 700 nm thick, as a n-type material using the appropriate designed mask as shown in Fig. 2c, and cool it to room temperature prior to the deposition of p- type of leg. The second step of device design is to deposit the p-type of semiconducting leg consisting of 700 nm of MoS<sub>2</sub> layer (Fig. 2e). At the end the metallic electrode of 70 nm chromium was deposited to interconnect the planar legs during electrical measurement (Fig. 2f). The final device was made out of 8 pairs of MoS<sub>2</sub> and WS<sub>2</sub> planar pattern to form the pn junction, usually exposed to the higher temperature end, and the metal contact connecting end, was exposed to lower temperature region.

**Characterization of the TE device.** The schematic set up that was used to measure the performance of pn-junction TEG device was made in the lab, as shown in Fig. 3. The apparatus involved for the measurement were hot plate, thermoelectric temperature control system, known resistor load, Keithley 2182 A nanovoltmeter, and forward looking infrared (FLIR A320) thermal camera. The TE device was placed in between the hot plate and a temperature control system, thermal grease was applied to ensure good thermal contact between the device and hot plate, and thermoelectric temperature control (TTC). During the measurement, the temperature of the hot plate was increased gradually while maintaining the cold side at 20 °C using TTC. The device was connected in series with a known resistance R<sub>1</sub>, and with the nanovoltmeter, which is configured to measure output voltage in the circuit. The voltage readings were taken at every temperature increment of a hot plate from 25.4 °C to 295 °C. The temperature of the cold region increased to 62 °C due to heat diffusion from hot to cold region.

## Results and Discussions

To study the crystalline quality of the films, X-ray diffraction was used. MoS<sub>2</sub> deposited by RF sputtering at T<sub>s</sub> = 450 °C revealed a pattern of a highly crystalline films with a strong orientation at 2θ = 13.6° that represents (002) MoS<sub>2</sub>, as shown in Fig. 4a. The peak at (002) shows crystal orientation with their basal planes parallel to the substrate surface<sup>36,37</sup>. However, high temperature annealing of the MoS<sub>2</sub> film at 600 °C and 700 °C (Ar<sub>2</sub> environment) for 1 hour improves the crystallinity quality a lot with sharp rise of the intensity up to four orders of magnitude as compare to as grown sample (450 °C). Further increase in the annealing temperature does not change any peak intensity or crystallinity of the film, but the thickness of the film start expanding with increasing in annealing temperature. Similarly, XRD graph of WS<sub>2</sub> Film shows a very strong crystal orientation of hexagonal (002) peak, as shown in Fig. 4b display. No other peaks are found in both films even at higher 2θ value except the Si substrate peak at 2θ = 33°.

Raman spectroscopy of 150 nm MoS<sub>2</sub> films deposited on Si (100) at T<sub>s</sub> = 400 °C is displayed in Fig. 5. There are two distinct peaks of E<sub>2g</sub><sup>1</sup>, and A<sub>1g</sub> located at 380 cm<sup>-1</sup> and 406 cm<sup>-1</sup>, corresponding to the characteristic feature

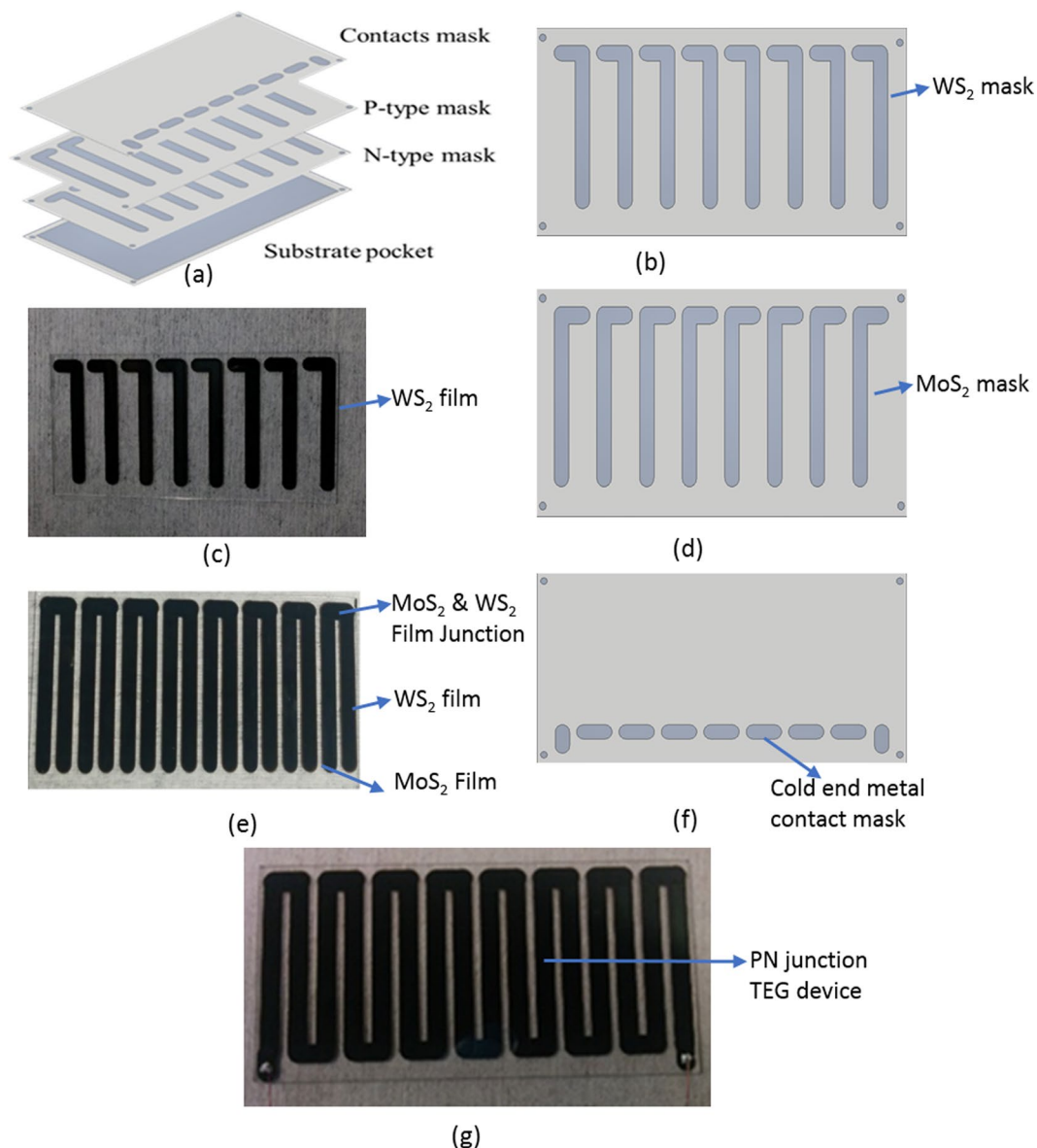


**Figure 2.** Schematic for step by step fabrication of thermoelectric pn junction device (a) Successive arrangement of different shadow mask for various materials deposited during device design. (b)  $WS_2$  leg mask set up on to the substrate prior to film deposition. (c)  $WS_2$  planar film considered as n-leg after deposition. (d) Arrangement of  $MoS_2$  mask for p-type planar leg onto the predisposed  $WS_2$  film. (e) Fabrication of  $MoS_2$  and  $WS_2$  film junction usually considered as hot end. (f) Alignment of mask for metal deposition to connect the other end of the both  $MoS_2$  and  $WS_2$  film. (g) PN junction based planar thermoelectric device structure.

of  $MoS_2$  film<sup>38–43</sup>. When the films were annealed at 600 °C and 700 °C in argon environment, we observe very interesting behavior and instead of shrinking, the film surprisingly start expanding from its original thickness and intensities of both vibrational modes increased as shown by the blue and the green curves. There is a clear redshift of  $E_{2g}^1$  and  $A_{1g}$  vibrational modes, relative to the as grown red curve when the films were annealed at 700 °C. Annealing improves significantly the  $MoS_2$  crystal quality structure and causes the removal of surface contaminants and/or strain relief<sup>40–42</sup>. Similarly, we also observe that the increase in film thickness, due to annealing, also affects the characteristic of the Raman peaks and the intensity of the two peaks prominently increases after annealing at 700 °C. The increase in intensity of  $E_{2g}^1$  mode is due to the increase in film thickness, however the increase in intensity of the  $A_{1g}$  mode is due to the change of force constant as a result of increasing number of layers, which has been studied elsewhere<sup>39,43</sup>. Furthermore, the microstructure of the sample also changes after annealing as shown in Supplementary Figs. (S1 and S2). The cross sectional view of the as grown and annealed  $MoS_2$  films are shown in Supplementary Fig. S3.

Atomic force microscopy of  $MoS_2$  films deposited at several substrate temperatures ( $T_s$ ) were studied and images are displayed in Fig. 6a–c. The films deposited on p-type Si (100) at  $T_s$  300 °C displayed rms of 4.22 nm, and those deposited at  $T_s$  150 °C displayed rms of 3.60 nm, and at room temperature deposition, the rms was

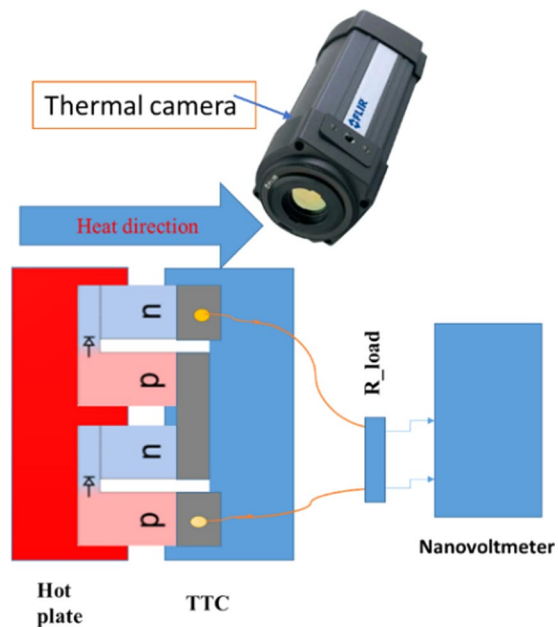


Figure 3. Hot plate and TTC Device testing set-up.

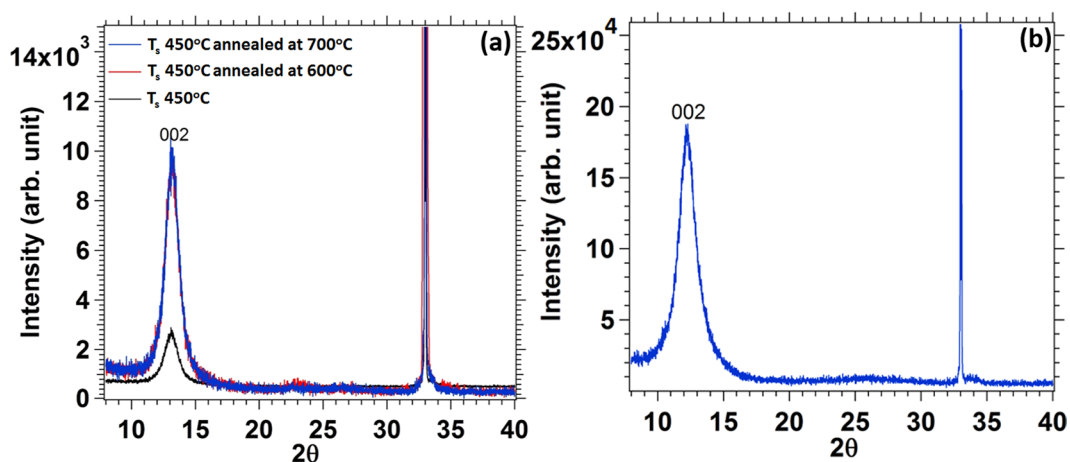


Figure 4. X-Ray diffraction graph of MoS<sub>2</sub> film deposited at 450°C and annealed at 600°C and 700°C for 1 hour at Ar<sub>2</sub> environment and (b) X-Ray diffraction graph of WS<sub>2</sub>.

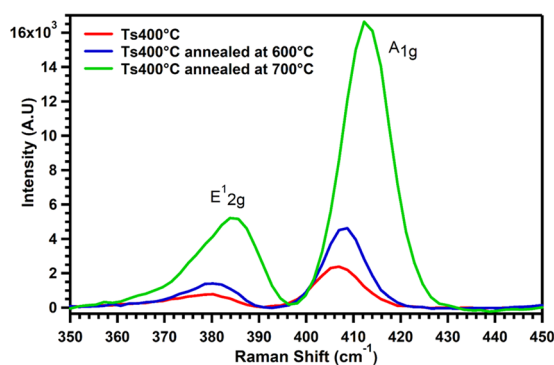
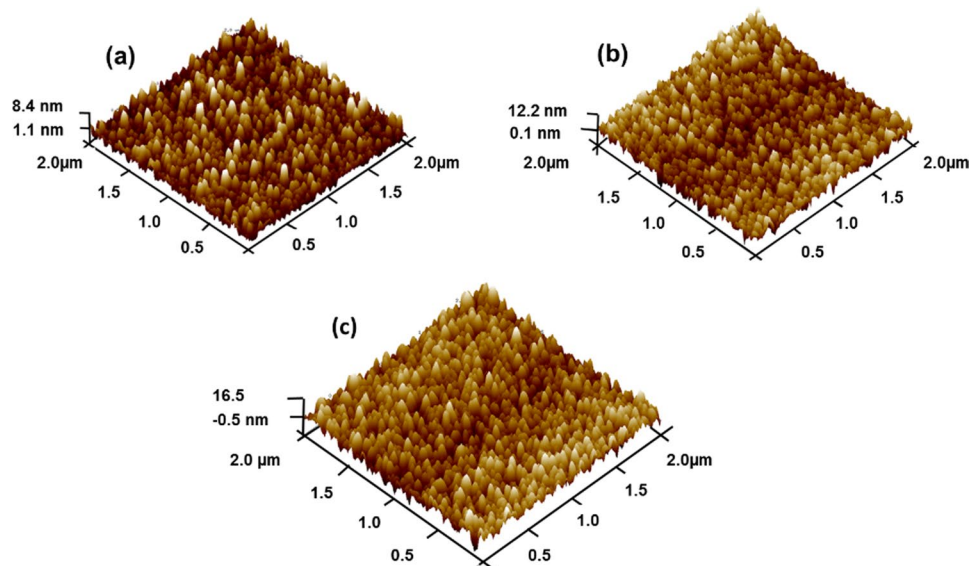


Figure 5. Raman spectra of MoS<sub>2</sub> films on silicon (100). The curves in blue and green color display the sample annealed at different temperatures.





**Figure 6.** Displays the AFM 3D images of MoS<sub>2</sub> film grown at (a) RT, (b) 150 °C and (c) 300 °C, respectively.

2.39 nm. AFM images of MoS<sub>2</sub> thin films show that the surface topography and crystal size distribution increase with increasing substrate temperature ( $T_s$ ). The reduction in rms was due to reduction in crystallization of the films when the temperature was lowered. The crystal size plays a role in the film properties. The surface roughness of the films has opposite effect in electrical conductivity of the films, in some cases the roughness leads to a reduction in electrical conductivity<sup>44</sup>. The roughness and grain boundaries cause additional scattering centers for conduction electrons leading to a higher electrical resistivity<sup>45</sup>. Figure 6a–c display 3D AFM images of MoS<sub>2</sub> films deposited on silicon.

The 2D images of the MoS<sub>2</sub> films deposited on silicon substrate at various temperature, are shown in Fig. 7a–c. The grains of the RT growth films are uniformly distributed on the surface of the sample with small amount of void present between the grains. However, the increase in growth temperature helps to develop larger grains of MoS<sub>2</sub> and the grain growth helps to reduce the void present among the grains. Furthermore, increase in substrate temperature favors to obtain a densely-packed grains over the MoS<sub>2</sub> film.

XPS analysis were used to study the binding energies of Mo and S atoms in MoS<sub>2</sub>. Table 1 shows XPS elemental analysis of MoS<sub>2</sub> films deposited on silicon substrate. Figure 8a shows wide scan of MoS<sub>2</sub> films. Binding energies of Mo 3d and S 2p in electrons volts are shown in Fig. 8b,c, respectively. Two distinct peaks at 229.4 eV and 232.7 eV are attributed to doublet; Mo 3d<sub>5/2</sub>, and Mo 3d<sub>3/2</sub>, respectively<sup>41–43</sup>. However, a small peak is observed at 236 eV is corresponding to Mo<sup>6+</sup> obtained from the formation of small amount MoO<sub>3</sub> in the MoS<sub>2</sub> film surface due to exposure to outside environment for longer period of time<sup>38</sup>. The peaks corresponding to S 2p state are shown in Fig. 8c, the two peaks located at 162.5 eV and 163.3 eV correspond to S 2p<sub>3/2</sub> and S 2p<sub>1/2</sub>, respectively. They represent orbital divalent sulfides ions (S<sup>2-</sup>)<sup>42–46</sup>. The observed peak positions of spin-orbit coupled Mo 3d and S 2p states are in agreement with the literature and confirms the synthesis of MoS<sub>2</sub> thin film<sup>38,43</sup>.

I–V characteristics of MoS<sub>2</sub> and WS<sub>2</sub> were measured at room temperature and shown in Fig. 9a,b. The inset represents the schematic of I–V measurement of the device. MoS<sub>2</sub> was deposited on n-type Si, while WS<sub>2</sub> on p-type Si with substrate temperature of 450 °C and annealed them at 600 °C in Argon environments for one hour. The thickness of the both films are 700 nm. Both had indium bottom contact and top chromium contacts, as shown in the insets. Both curves display rectifying characteristics at a turn on voltage ( $V_{on}$ ) of 0.2 V where the current starts to increase infinitely<sup>43,47,48</sup>.

Seebeck coefficient of MoS<sub>2</sub> was performed from 300 K to 430 K at a temperature interval of 5 K using digital Seebeck controller measurement set up (Make-MMR technologies, model- SB1000). During the measurement the temperature difference ( $\Delta T$ ), between the hot and cold regions, was between 4 to 5 K. Figure 10a, displays the Seebeck coefficient temperature dependence. The positive Seebeck coefficient represents majority of hole carriers which are present in MoS<sub>2</sub> films typical for p-type semiconductor material<sup>49–51</sup>. Temperature dependent resistivity of the films was performed using linear four-probe technique from room temperature to 420 K. During the measurement a fixed current of 1 mA was applied between the outer two probes using a Keithley 6220 precision current source. The voltage was measured using a Keithley 2182 A nanovoltmeter. Figure 10b displays the resistivity/conductivity of MoS<sub>2</sub> films. The films display semiconducting behavior.

The power factor was calculated using the product of Seebeck coefficient squared and electrical conductivity ( $pf = S^2\sigma$ ) measured from RT to 430 K. The results display strong temperature dependence, where it increases with temperature until a maximum value of  $1.15 \times 10^{-3} \text{ Wm}^{-1} \text{ K}^{-2}$  is reached at 370 K, as shown in Fig. 10c below, before it started to decrease.

Thermal conductivity of MoS<sub>2</sub> was measured at room temperature using time domain thermal reflectance (TDTR) at modulation frequency of 0.824–9.68 MHz. An Aluminum transducer layer of 88 nm was deposited on

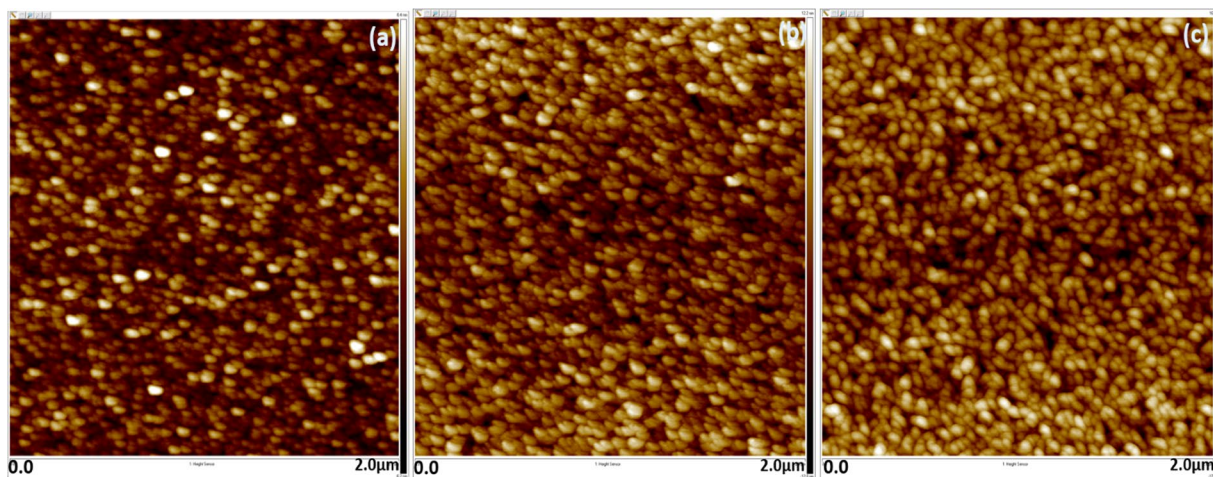


**Figure 7.** AFM 2D images of MoS<sub>2</sub> film grown at (a) RT, (b) 150 °C and (c) 300 °C, respectively.

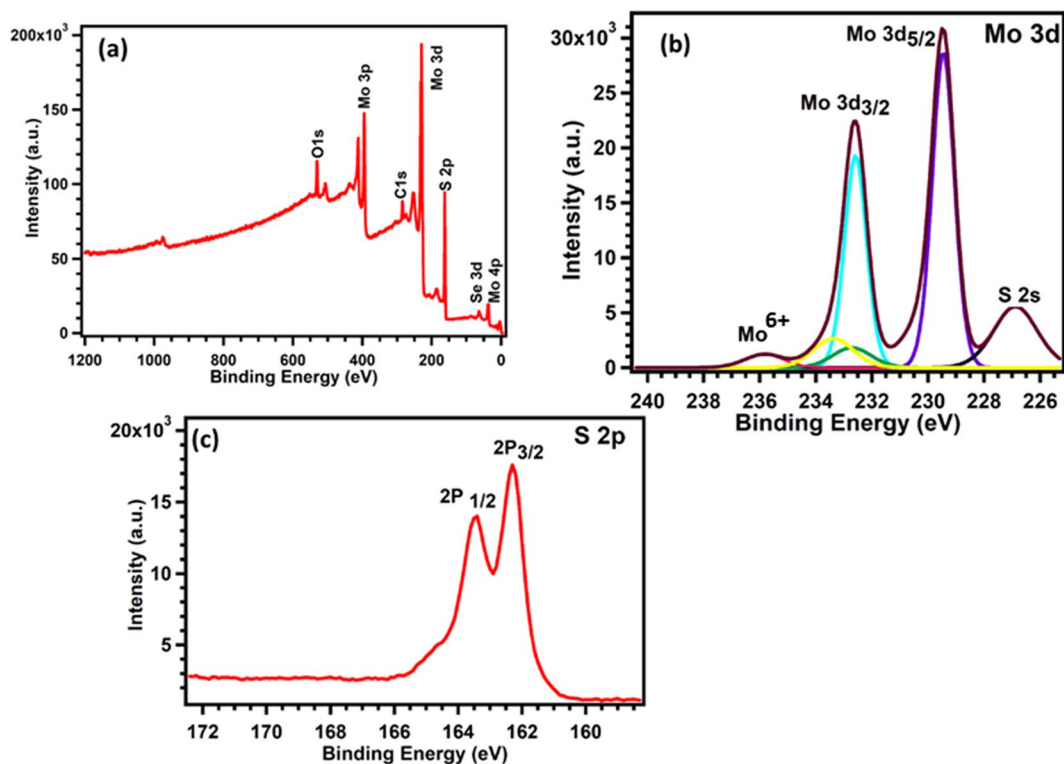


**Figure 8.** The X-ray photoelectron spectroscopy of MoS<sub>2</sub> films: (a) XPS survey spectrum (b) High resolution XPS spectrum of Mo 3d peaks, and (c) High resolution XPS spectrum of the S 2p peaks levels.

Peak	Type	Position BE(eV)	FWHM (eV)	Raw Area (cps eV)	RSF	Atomic Mass	Atomic Conc. %	Mass Conc. %
C 1 s	Reg	284.403	1.459	3632.4	0.278	12.011	14.61	4.21
O 1 s	Reg	530.803	1.977	9066.5	0.78	15.999	12.01	4.61
Si 2p	Reg	107.303	10.8	0	0.328	28.086	0	0
Mo 3d	Reg	229.403	0.894	66103.1	3.321	95.922	22.63	52.11
S 2p	Reg	162.303	1.919	29287	0.668	32.065	50.75	39.07

**Table 1.** Elemental analysis of MoS<sub>2</sub> films.

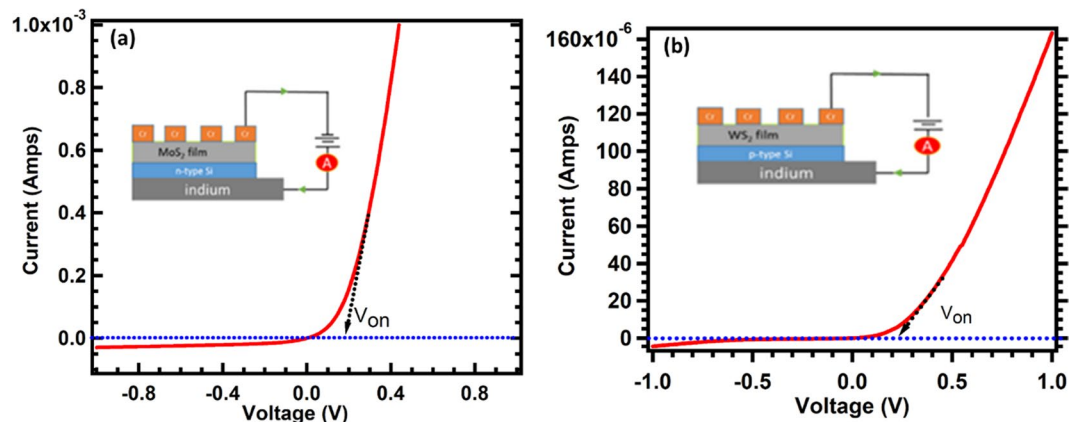


**Figure 9.** (a,b) Display the I-V characteristics of MoS<sub>2</sub> and WS<sub>2</sub>, respectively. The inset shows the schematic illustration setup of the electrical measurement of the MoS<sub>2</sub>/n-type silicon, and indium as the bottom contact.

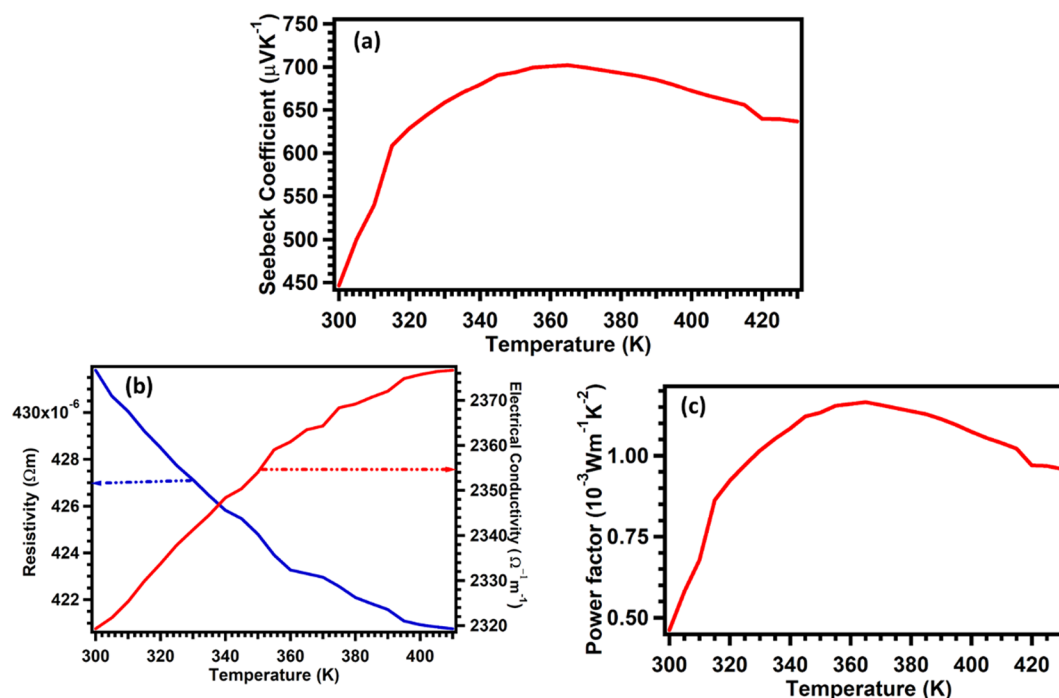


**Figure 10.** Thermoelectric transport properties of MoS<sub>2</sub>. (a–c) Display Seebeck coefficient, electrical measurement, and power factor of MoS<sub>2</sub>, respectively.

Seebeck Coeff. ( $\mu\text{VK}^{-1}$ )	Electrical Conductivity ( $\Omega^{-1}\text{m}^{-1}$ )	Thermal Conductivity ( $\text{Wm}^{-1}\text{K}^{-1}$ )	Temperature (K)	Figure of merit
466.34	2320	0.07–0.50	300	0.27–1.98

**Table 2.** Calculated figure merit.

850 nm thick MoS<sub>2</sub> sample to serve as an energy absorber for the laser beams as well as temperature transducer for the probe beam<sup>52</sup>. The films deposited on glass substrates displays low cross-plane thermal conductivity of 0.07–0.5 W/mK at 300 K. The calculated figure of merit of highly crystalline MoS<sub>2</sub> films, assuming the thermal conductivity is approximately isotropic, was approximately 0.27–1.98 at 300 K, as shown in Table 2. At the high end, this value is higher than the most efficient thermoelectric materials, such as Bi<sub>2</sub>Te<sub>3</sub> with its value approximately < 1 at room temperature<sup>53</sup>. The reduction of thermal conductivity is due to the surface roughness that interacts with a broadband spectrum of phonons resulting in decreased thermal conductivity due to frequency dependent scattering<sup>45,54–56</sup>. Additionally, the effect of low thermal conductivity is attributed to grain size and grain boundaries that act as phonon scattering centers<sup>57</sup>.



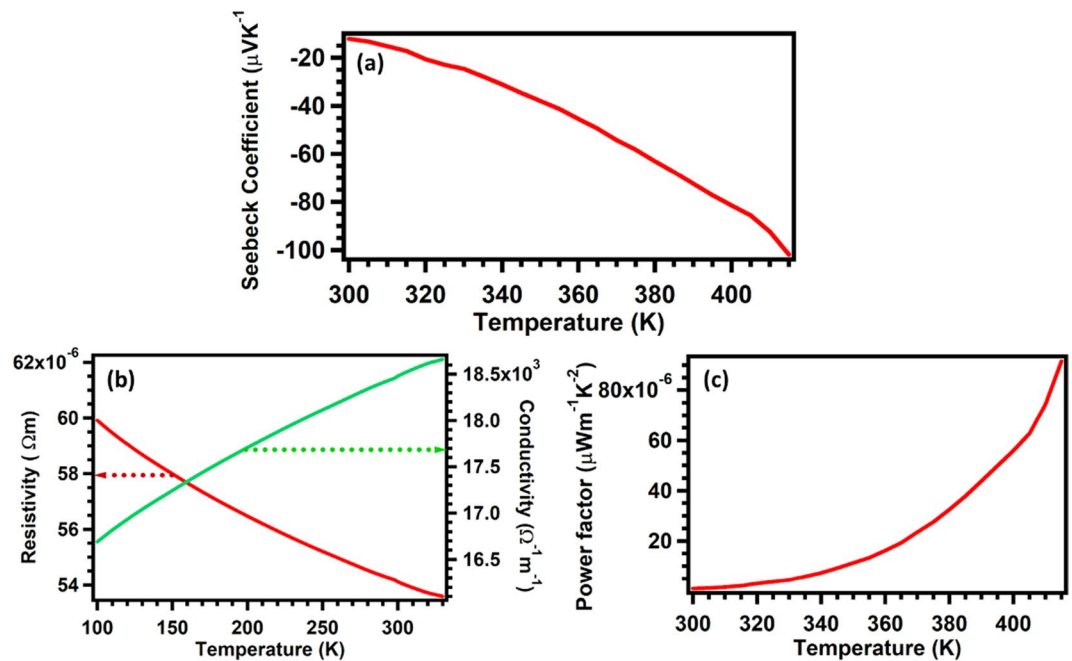


**Figure 11.** Thermoelectric transport properties of  $\text{WS}_2$ . (a–c) Display Seebeck coefficient, resistivity and power factor of  $\text{WS}_2$  films.

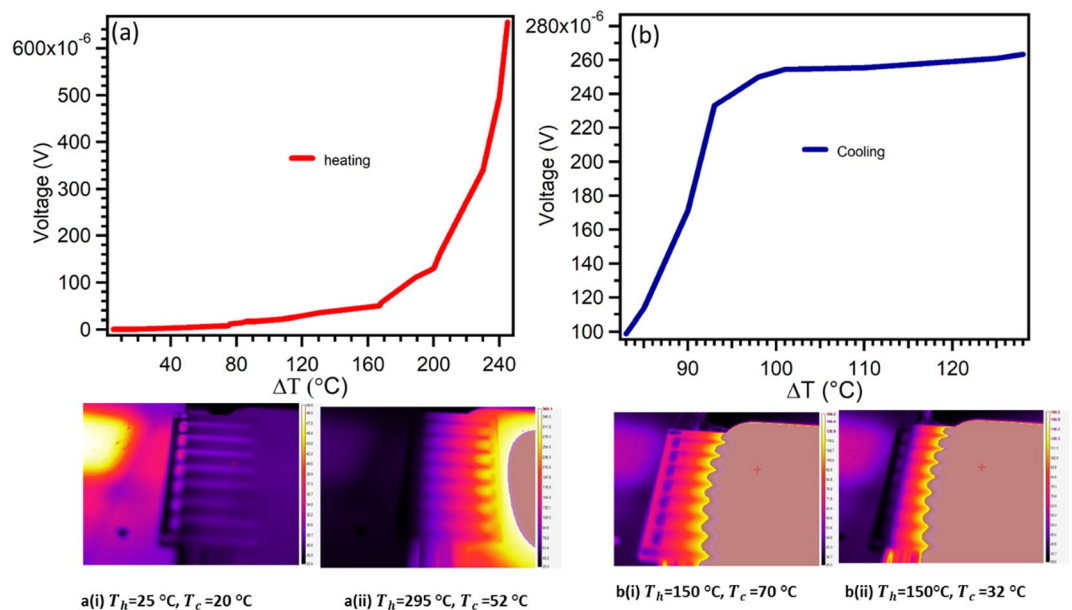


**Figure 12.** Voltage measurement. (a,b) Heating and cooling of TE device ( $\text{MoS}_2$ - $\text{WS}_2$ ), respectively.

Seebeck coefficient of  $\text{WS}_2$  was measured from 300 K to 420 K, as shown in Fig. 11a. The absolute value of Seebeck coefficient increases with temperature, exhibiting negative thermo-power, implying that electrons are the majority carriers in the  $\text{WS}_2$  films, which is normal for n-type material. Resistivity measurements exhibit semiconductor behavior, as shown in Fig. 11b, while the power factor increases with temperature, Fig. 11c.

Figure 12a,b display temperature gradient versus output voltage of a thin film pn-junction TE device ( $\text{MoS}_2$  (p-type) and  $\text{WS}_2$  (n-type)) for both heating and cooling. Voltage increases with increase in temperature gradient. For the device heating experiment, TTC was set at 20 °C whereas the hot plate temperature was set to start at 25 °C. The temperature of the hot side was increased gradually until 295 °C, as seen by thermal camera images of Fig. 12a (i, and ii). During cooling, the hot plate temperature was maintained at 150 °C, while the TTC was set to start decreasing from 70 °C to 32 °C, as shown in thermal camera image of Fig. 12b (i, and ii). The cooling testing shows that the planar thin film device is actively used for cooling up to  $\Delta T$  of 95 °C, as seen by steeper curve in

**Fig. 12b.** Device heating voltage of 0.7 mV was achieved when temperature gradient was 240 °C. Whereas cooling produced a voltage of 0.27 mV at a temperature gradient of 118 °C.

## Discussion

We have successfully demonstrated large-area highly crystalline MoS<sub>2</sub> thin films deposited on different substrates via RF magnetron sputtering technique. XRD revealed highly oriented (001) films and AFM display shows the homogenous distribution of MoS<sub>2</sub> grain on the Si substrate. MoS<sub>2</sub> films revealed ultralow thermal conductivity of 0.07 W/mK at 300 K, which is a good candidate for thermoelectric applications. Additionally, pn junction TEG based on MoS<sub>2</sub> (p-type) and WS<sub>2</sub> (n-type) planner structure demonstrates superior energy harvesting and cooling performance compared to convention TEG, where metal contacts are done on both hot region and cold region. The crystalline quality of the films was improved via annealing at 600 °C and 700 °C in an argon environment. This produced increased intensity and red shifted of  $E_{2g}^1$  and  $A_{1g}$  Raman peaks.

## Conclusion

We have studied thermoelectric transport properties of highly crystalline MoS<sub>2</sub> films as well as WS<sub>2</sub> films deposited by RF magnetron sputtering for high-efficient thermal energy harvesting applications. AFM images display an increase in rms when MoS<sub>2</sub> films were grown at higher substrate temperatures. Surface roughness of the films has opposite effect in electrical conductivity and thermal properties of the films. Roughness and grain boundaries leads to an increase in resistivity of the films. MoS<sub>2</sub> films indicate low thermal conductivity and a Seebeck coefficient of 446.342 μV/K, suggesting a figure of merit of up to 1.98 at 300 K. Also the thermoelectric generator fabricated based on pn-junction at the hot end and chromium contacts at the cold end demonstrates superior efficiency performance at high temperature gradients, due to generation of electrons–holes at the depletion region of the pn-junction. In addition, the pn-junction makes the device more robust at higher temperatures by withstanding thermal-mechanical stress, alloying, inter diffusion of atoms, and mismatch of coefficients of thermal expansion between the materials in contact at the hot side. Device heating voltage of 0.7 mV was realized at a temperature gradient of 240 °C. Whereas cooling produced a voltage of 0.27 mV at a temperature gradient of 118 °C. These promising results suggest that the material can potential be used for moderate waste heat harvesting.

## Methods

**The film growth.** Both WS<sub>2</sub> and MoS<sub>2</sub> thin films were grown from the target materials by physical vapor deposition technique using radio frequency magnetron sputtering on to the various substrates. Prior to the deposition, all the substrates were cleaned thoroughly by dipping them to different solvent such as acetone, methanol and isopropanol for 5 minutes each solution in ultrasonic bath. Then the substrate were cleaned using deionized water and followed by dried them in nitrogen gun. High purity targets of MoS<sub>2</sub> and WS<sub>2</sub> (99.99% purity) were used as source materials and cleaned them in Ar<sub>2</sub> plasma environment for 20 minutes to remove any oxide/contaminants from the target surface. All the substrate were transferred to high vacuum  $1.6 \times 10^{-6}$  Torr deposition chamber for the optimum thickness of MoS<sub>2</sub> and WS<sub>2</sub> thin film grown. The growth parameter for MoS<sub>2</sub> films were 2.3 mTorr Ar<sub>2</sub> pressure, 150 W plasma power. Whereas WS<sub>2</sub> films were grown at 5mTorr Ar<sub>2</sub> pressure, 150 W plasma power. All the films are grown for different period of time from 10–45 minutes to obtain various film thickness. The films were annealed at 600 °C and 700 °C under argon atmosphere at a flow rate of 50 sccm to improve the crystallinity of the films<sup>35</sup>.

**Fabrication of pn-junction TE device.** The PN junction based thermoelectric devices were fabricated using different shadow mask and proper alignment of the planar leg. All the step by step masks were designed by cutting thin sheet of steel using local workshop. The films were grown at high vacuum and much above room temperature and precaution were taken to avoid contamination. The devices was fabricated on glass substrate; first WS<sub>2</sub> films were deposited followed by MoS<sub>2</sub> films to make pn junction at one end of the structure which is considered as a hot end. Other end of the WS<sub>2</sub> and MoS<sub>2</sub> legs were connected using 60 nm of Cr metal contact using thermal evaporation technique<sup>35</sup>.

**Characterization details of MoS<sub>2</sub> and WS<sub>2</sub> films.** Synthesis of MoS<sub>2</sub> films were analyzed by Raman spectroscopy (LabRAM HR Evolution, 532 nm laser) with a spot size of 1 μm and acquisition time of 300 seconds. A silicon substrate with a Raman peak of  $520.6 \text{ cm}^{-1}$  offset: 478 and coefficient of  $6.07 \times 10^{-3}$  was used to calibrate the instrument. The crystallinity of the films was measured by X-ray diffractometer (XRD, Rigaku) using Cu K<sub>α</sub> X-ray source operated at 20 kV, and 40 mA. Photoelectron spectroscopy (XPS) was used to study the elemental analysis of Mo and S atoms. To study morphology and grain size atomic force microscopy (AFM) (Veeco, Dimension Icon Scan Asyst) was used. Thermoelectric properties and Seebeck coefficient was measured using MMR technologies. Resistivity/conductivity was measured using standard four-probe technique (APD cryogenics). IV measurements were measured using Keithley 4200-SCS (semiconductor characterization system). Total thermal conductivity was measured using TDTR, operated at modulation frequency of 0.824–9.68 MHz. For temperature dependent electrical study, the samples are inserted into the cryostat and standard linear four-probe technique was used for data acquisition<sup>35</sup>.

Received: 4 September 2018; Accepted: 18 October 2019;

Published online: 23 January 2020

## References

- Sundarraaj, P., Maity, D., Roy, S. S. & Taylor, R. A. Recent advances in thermoelectric materials and solar thermoelectric generators – a critical review. *RSC Adv.* **4**, 46860–46874 (2014).
- Liu, W., Yan, X., Chen, G. & Ren, Z. Recent advances in thermoelectric nanocomposites. *Nano Energy* **1**, 42–56 (2012).
- Snyder, G. J. & Toberer, E. S. I. Complex thermoelectric materials. *Nat. Mater.* **7**, 105–114 (2008).
- Tritt, T. M. & Subramanian, M. Thermoelectric Materials, Phenomena, and Applications: A Bird's Eye View. *MRS Bull.* **31**, 188–198 (2006).
- Kim, W. *et al.* Thermal conductivity reduction and thermoelectric figure of merit increase by embedding nanoparticles in crystalline semiconductors. *Phys. Rev. Lett.* **96**, 1–4 (2006).
- Snyder, G. J. & Toberer, E. S. Complex thermoelectric materials. *Nat. Mater.* **7**, 105–114 (2008).
- Chen, Z. G., Hana, G., Yanga, L., Cheng, L. & Zou, J. Nanostructured thermoelectric materials: Current research and future challenge. *Prog. Nat. Sci. Mater. Int.* **22**, 535–549 (2012).
- Mahan, G. D. & Sofo, J. O. The best thermoelectric. *Proc. Natl. Acad. Sci.* **93**, 7436–7439 (1996).
- Hicks, L. D. & Dresselhaus, M. S. Effect of quantum-well structures on the thermoelectric figure of merit. *Phys. Rev. B* **47**, 12727–12731 (1993).
- Capinski, W. S. *et al.* Thermal-conductivity measurements of GaAs/AlAs superlattices using a picosecond optical pump-and-probe technique. *Phys. Rev. B* **59**, 8105–1113 (1999).
- Venkatasubramanian, R. Lattice thermal conductivity reduction and phonon localization like behavior in superlattice structures. *Phys. Rev. B* **61**, 3091–3097 (2000).
- Borca-Tasciuc, T. *et al.* Thermal conductivity of symmetrically strained Si/Ge superlattices. *Superlattices Microstructures* **28**, 199–206 (2000).
- He, M. *et al.* Thermopower enhancement in conducting polymer nanocomposites via carrier energy scattering at the organic–inorganic semiconductor interface. *Energy Environ. Sci.* **5**, 8351–8358 (2012).
- Bahk, J. H., Santhanam, P., Bian, Z. X., Ram, R. & Shakouri, A. Resonant carrier scattering by core-shell nanoparticles for thermoelectric power factor enhancement. *Appl. Phys. Lett.* **100**, 012102 (2012).
- Li, J. H. *et al.* BiSbTe-based nanocomposites with high ZT: the effect of SiC nanodispersion on thermoelectric properties. *Adv. Funct. Mater.* **23**, 4317–4323 (2013).
- Venkatasubramanian, R., Siivola, E., Colpittes, T. & O'Quinn, B. Thin-film thermoelectric devices with high room-temperature figures of merit. *Nat.* **413**, 597–602 (2001).
- Wickramaratne, D., Zahid, F. & Lake, R. K. Electronic and thermoelectric properties of few-layer transition metal dichalcogenides. *J. Chem. Phys.* **140**, 124710 (2014).
- Lee, C., Hong, J., Whangbo, M. H. & Shim, J. H. Enhancing the Thermoelectric Properties of Layered Transition-Metal Dichalcogenides 2H-MQ<sub>2</sub> (M = Mo, W; Q = S, Se, Te) by Layer Mixing: Density Functional Investigation. *Chem. Mater.* **25**, 3745–3752 (2013).
- Fan, D. D. *et al.* MoS<sub>2</sub> nanoribbons as promising thermoelectric materials. *Appl. Phys. Lett.* **105**, 133113 (2014).
- Guo, H., Yand, T., Tao, P., Wang, Y. & Zhang, Z. High pressure effect on structure, electronic structure, and thermoelectric properties of MoS<sub>2</sub>. *J. Appl. Phys.* **113**, 013709 (2013).
- Huang, W., Da, H. & Liang, G. Thermoelectric performance of MX<sub>2</sub> (M = Mo, W; X = S, Se) monolayers. *J. Appl. Phys.* **113**, 104304 (2013).
- Zhang, Z., Xie, Y., Peng, Q. & Chen, Y. A theoretical prediction of super high performance thermoelectric materials based on MoS<sub>2</sub>/Ws<sub>2</sub> hybrid nanoribbons. *Sci. Rep.* **6**, 21639–1–8 (2016).
- Baugher, B. W., Churchill, H. O., Yang, Y. & Jarillo-Herrero, P. Intrinsic electronic transport properties of high-quality monolayer and bilayer MoS<sub>2</sub>. *Nano Lett.* **13**, 4212–4216 (2013).
- Gu, X. & Yang, R. Phonon transport in single-layer transition metal dichalcogenides: A first-principles study. *Appl. Phys. Lett.* **105**, 131903 (2014).
- Peng, Q. & De, S. Outstanding mechanical properties of monolayer MoS<sub>2</sub> and its application in elastic energy storage. *Phys. Chem. Chem. Phys.* **15**, 19427–19437 (2013).
- Dresselhaus, M. S. *et al.* New directions for low-dimensional thermoelectric materials. *Adv. Mater.* **19**, 1043–1053 (2007).
- Kraemer, D. *et al.* High-performance flat-panel solar thermoelectric generators with high thermal concentration. *Nat. Mater.* **10**, 532–538 (2011).
- Abdel-motaleb, I. M. & Qadri, S. M. Thermoelectric Devices: Principles and Future Trends. 1–20.
- Yang, F., Zheng, S., Wang, H., Chu, W. & Dong, Y. A thin film thermoelectric device fabricated by a self-aligned shadow mask method. *J. Micromechanics Microengineering* **27** (2017).
- Mizoshiri, M., Mikami, M. & Ozaki, K. The effect of Cr buffer layer thickness on voltage generation of thin-film thermoelectric modules. *J. Micromechanics Microengineering* **23** (2013).
- Bell, L. E. Cooling, Heating, Generating Heat with and Recovering Waste Thermoelectric. *Sci.* **321**, 1457–1461 (2014).
- Takashiri, M., Shirakawa, T. & Miyazaki, K. O. H. Thermoelectric Properties of Bismuth-Telluride Thin Films and Their Thermoelectric Generators. **9**, 261–271 (2007).
- Becker, A., Chavez, R., Petermann, N., Schierning, G. & Schmechel, R. A thermoelectric generator concept using a p-n junction: Experimental proof of principle. *J. Electron. Mater.* **42**, 2297–2300 (2013).
- Archibald, S. *et al.* Ac ce pte d M us pt. *Geophys. Res. Lett.* In press (2017).
- Kogo, G. *et al.* Highly-efficient thermoelectric pn-junction device based on bismuth telluride (Bi<sub>2</sub>Te<sub>3</sub>) and molybdenum disulfide (MoS<sub>2</sub>) thin films fabricated by RF magnetron sputtering technique. *J. Appl. Phys.* **124**, 165106–1–9 (2018).
- Moser, J., Lévy, F. & Bussy, F. Composition and growth mode of MoS<sub>x</sub> sputtered films. *J. Vac. Sci. Technol. A Vacuum, Surfaces, Film.* **12**, 494–500 (1994).
- Wang, B. *et al.* Mechanical properties of RF-sputtering MoS<sub>2</sub> thin films Mechanical properties of RF-sputtering MoS<sub>2</sub> thin films. *Surf. Topogr.: Metrol. Prop.* **5**, 025003 (2017).
- Dhyani, V. & Das, S. High-Speed Scalable Silicon-MoS<sub>2</sub> P-N Heterojunction Photodetectors. *Sci. Rep.* **7**, 44243 (2017).
- Han, S. A., Bhatia, R. & Kim, S.-W. Synthesis, properties and potential applications of two-dimensional transition metal dichalcogenides. *Nano Converg.* **2**, 17 (2015).
- Liu, K. K. *et al.* Growth of large-area and highly crystalline MoS<sub>2</sub> thin layers on insulating substrates. *Nano Lett.* **12**, 1538–1544 (2012).
- Kaplan, D., Mills, K., Lee, J., Torrel, S. & Swaminathan, V. Excitation intensity dependent photoluminescence of annealed two-dimensional MoS<sub>2</sub> grown by chemical vapor deposition. *J. Appl. Phys.* **119**, 214301–1–5 (2016).
- Hussain, S. *et al.* Large-area, continuous and high electrical performances of bilayer to few layers MoS<sub>2</sub> fabricated by RF sputtering via post-deposition annealing method. *Sci. Rep.* **6**, 1–13 (2016).
- Pradhan, S. K., Xiao, B. & Pradhan, A. K. Enhanced photo-response in p-Si/MoS<sub>2</sub> heterojunction-based solar cells. *Sol. Energy Mater. Sol. Cell* **144**, 117–127 (2016).
- Timoshevskii, V., Ke, Y., Guo, H. & Gall, D. The influence of surface roughness on electrical conductance of thin Cu films: An ab initio study. *J. Appl. Phys.* **103**, 9–12 (2008).

45. Kim, Y. S., Sung, M. Y., Lee, Y. H., Ju, B. K. & Oh, M. H. The Influence of Surface Roughness on the Electric Conduction Process in Amorphous Ta<sub>2</sub>O<sub>5</sub> Thin Films. *J. Electrochem. Soc.* **146**, 3398–3402 (1999).
46. Moulder, J. F., Stickle, W. F., Sobol, P. E. & Bomben, K. D. Handbook of X-ray Photoelectron Spectroscopy Edited by. 261 (1992).
47. Liu, Y. *et al.* Electrical and photovoltaic characteristics of MoS<sub>2</sub>/Si p-n junctions. *J. Appl. Phys.* **117**, 114502 (2015).
48. Hao, L. *et al.* High hydrogen sensitivity of vertically standing layered MoS<sub>2</sub>/Si heterojunctions. *J. Alloy. Compd.* **682**, 29–34 (2016).
49. Huang, W., Da, H. & Liang, G. Thermoelectric performance of MX<sub>2</sub> (M Mo,W; X S, Se) monolayers. *J. Appl. Phys.* **113**, 104304 (2013).
50. Guo, H. H., Yang, T., Tao, P. & Zhang, Z. D. Theoretical study of thermoelectric properties of MoS<sub>2</sub>. *Chinese Phys. B* **23**, 017201-1-7 (2014).
51. Huang, W., Luo, X., Gan, C. K., Quek, S. Y. & Liang, G. Theoretical study of thermoelectric properties of few-layer MoS<sub>2</sub> and WSe<sub>2</sub>. *Phys. Chem. Chem. Phys.* **16**, 10866 (2014).
52. Liu, J. *et al.* Simultaneous measurement of thermal conductivity and heat capacity of bulk and thin film materials using frequency-dependent transient thermoreflectance method Simultaneous measurement of thermal conductivity and heat capacity of bulk and thin film materi. *Rev. Sci. Instrum.* **034902**, 1–12 (2013).
53. Takashiri, M., Takiishi, M., Tanaka, S., Miyazaki, K. & Tsukamoto, H. Thermoelectric properties of n-type nanocrystalline bismuth-telluride-based thin films deposited by flash evaporation. *J. Appl. Phys.* **101**, 074301 (2007).
54. Lim, J., Hippalgaonkar, K., Andrews, S. C., Majumdar, A. & Yang, P. Quantifying surface roughness effects on phonon transport in silicon nanowires. *Nano Lett.* **12**, 2475–2482 (2012).
55. Chen, G. Size and Interface Effects on Thermal Conductivity of Superlattices and Periodic Thin-Film Structures. *J. Heat. Transf.* **119**, 220–229 (1997).
56. Morikawa, S., Inamoto, T. & Takashiri, M. Thermoelectric properties of nanocrystalline Sb<sub>2</sub>Te<sub>3</sub> thin films: experimental evaluation and first-principles calculation, addressing effect of crystal grain size. *Nanotechnol.* **29**, 075701 (2018).
57. Soyez, G. *et al.* Grain-size-dependent thermal conductivity of nanocrystalline yttria-stabilized zirconia films grown by metal-organic chemical vapor deposition. *Appl. Phys. Lett.* **77**, 1155–1157 (2000).

## Acknowledgements

This work is supported by the NSF-CREST (CNBMD) grant number HRD 1036494 CREST CREAM HRD-1547771. Authors are thankful to Dr. Donley Carrie Lynn for XPS measurements, Dr. Jonathan Skuza for experimental help and guidance, Prof. Ali Shakouri and Yee Rui Koh for help with thermal conductivity measurement. We sincerely thank Mr. Richard Dyer (Norfolk Public Schools-NTC) for assistance in the machine shop and Lauren Anderson for proof-reading the manuscript.

## Author contributions

G.K. and S.K.P. wrote the main manuscript text, experimental work, and data analysis, M.B. project planning, S.K.P., B.X. and M.B. experimental guidance and manuscript edit, S.K.P., A.M. and A.C. experimental work and data analysis, K.Y., G.K., S.D., H.L. and J.N. device fabrication design and substrates preparation. Both G.K. and S.K.P. has equal contribution in this work.

## Competing interests

The authors declare no competing interests.

## Additional information

**Supplementary information** is available for this paper at <https://doi.org/10.1038/s41598-020-57991-y>.

**Correspondence** and requests for materials should be addressed to G.K. or S.K.P.

**Reprints and permissions information** is available at [www.nature.com/reprints](http://www.nature.com/reprints).

**Publisher's note** Springer Nature remains neutral with regard to jurisdictional claims in published maps and institutional affiliations.



**Open Access** This article is licensed under a Creative Commons Attribution 4.0 International License, which permits use, sharing, adaptation, distribution and reproduction in any medium or format, as long as you give appropriate credit to the original author(s) and the source, provide a link to the Creative Commons license, and indicate if changes were made. The images or other third party material in this article are included in the article's Creative Commons license, unless indicated otherwise in a credit line to the material. If material is not included in the article's Creative Commons license and your intended use is not permitted by statutory regulation or exceeds the permitted use, you will need to obtain permission directly from the copyright holder. To view a copy of this license, visit <http://creativecommons.org/licenses/by/4.0/>.

© The Author(s) 2020